1D and 2D simulations for the NASA Electric Arc Shock Tube experiments

By D.V. Kotov, H.C. Yee, M. Panesi, D. Prabhu, AND A. Wray

1. Motivation and objectives

The Electric Arc Shock Tube (EAST) facility at NASA Ames Research Center is used to generate high-enthalpy gas tests for studying high-speed atmospheric entry physics. The facility is composed of a long tube and a chamber. In the chamber, which contains a driver gas, an electrical discharge takes place, giving rise to a sudden increase of the gas temperature and pressure. The chamber's geometry can be approximated as a 10-cm cylindrical tube though its real geometry is more complex and not axisymmetric. An aluminum diaphragm separates the driver from the driven gas. At the high pressure generated by the discharge, the diaphragm bursts, forming a shock wave that travels at high speed through a long cylindrical tube, 10 cm in diameter. As the shock propagates downstream, the shock-heated gas radiates, and in a test section emission spectroscopy is used to determine the radiative signature and thereby the thermo-chemical and radiative properties of the medium.

The experiments being simulated here make use of helium as a driver gas and synthetic air (N_2 + O_2) as a test gas (or driven gas). The shock velocities obtained in EAST experiments range between 9 and 16 km/sec. The distance between the diaphragm and the test section is 7.0 m. At the test section the spectrally and spatially resolved shock-layer radiance is analyzed by taking a snapshot of the shock wave and the following gas as they pass in front of an optical access window.

It is important to note that optically probing the shocked gas does not provide any information about the radial structure of the flow in the shock tube. The experiments only provide integrated measurements that include all the absorption and emission across the tube. Experimental data processing currently conducted at NASA Ames takes the flow to be one-dimensional, and any boundary layer effects are neglected. In reality, however, viscous effects may significantly impact the interpretation of the tests. To make better use of the flow radiation measurements one needs to know the radiative properties within the boundary layer, which can be estimated by numerical simulations.

However there are some challenges in a CFD computation of this problem. One major challenge lies in the specification of the thermochemical state of the arc-heated driver gas, i.e., the initial state. Although energy deposition into the driver gas is time dependent, the current approach has been to adjust a constant temperature until the target shock velocity is reproduced.

Several other challenges arise from the need to accurately capture the spatial-temporal evolution of the flow field in order to properly characterize boundary layer growth on the shock tube wall. The boundary layer is the primary cause of the shock wave's deceleration, and it has important implications for re-absorption of shock layer radiation prior to instrument detection. These phenomena are unsteady and must be treated as such. For flight experiments one usually seeks a steady state solution, so that the simulation is not constrained by time accuracy requirements, and various acceleration techniques

can be used. The shock tube flowfield, however, develops in time and thus requires, at a minimum, second order time integration and minimization of numerical instabilities due to the multiscale physics and stiff source terms of the flow. Similarly, the spatial relaxation scale has to be resolved accurately, and all wave interactions have to be accounted for. Initial simulations of the EAST facility have demonstrated strong sensitivity to the choice of numerical method. Therefore, schemes with high-order spatial accuracy and low dissipation are desired. Furthermore, the length of the EAST facility is roughly 8 m, which translates to enormous grids. The combination of these temporal and spatial resolution requirements demands significant computer resources and simulation time to account for all important phenomena.

An additional, less well-known challenge involves the stiffness of the source terms in the governing equations. The temperature in the shock during the experiment is above $20,000\ K$, which means that chemical reaction rates in the vicinity of the shock become very high and the source term describing the chemical reactions becomes stiff. As most common shock-capturing schemes have been developed for problems without source terms, when applied to problems with nonlinear and/or stiff source terms these methods can result in spurious solutions, even when solving a conservative system of equations with a conservative scheme. This kind of behavior can be observed even for a scalar case (LeVeque & Yee 1990) as well as for the case with two species and one reaction (Wang *et al.* 2012). For further information concerning this issue see (LeVeque & Yee 1990; Griffiths *et al.* 1992; Lafon & Yee 1996; Yee *et al.* 2011, 2012).

For a brief introduction and earlier CFD simulations of EAST see (Yee *et al.* 2012; McCorkle & Hassan 2010). Because of the non-symmetrical geometry of the driver zone, partially due to the opening of the diaphragm and the non-symmetrical configuration of the discharge, a full 3D computation should be carried out for this problem. The present investigation is to perform less CPU-time-intensive 1D and 2D computations for the purpose of gaining first-hand understanding of the simulation challenges involved. Knowledge gained will provide guidance for future 3D CFD simulations.

2. Governing equations

Consider the 3D reactive Navier-Stokes equations for a one-temperature energy model:

$$\frac{\partial \rho_s}{\partial t} + \frac{\partial}{\partial x_j}(\rho_s u_j + \rho_s d_{sj}) = \Omega_s \qquad (2.1)$$

$$\frac{\partial}{\partial t}(\rho u_i) + \frac{\partial}{\partial x_j}(\rho u_i u_j + p\delta_{ij} - \tau_{ij}) = 0 \qquad (2.2)$$

$$\frac{\partial}{\partial t}(\rho E) + \frac{\partial}{\partial x_j}(u_j(\rho E + p) + q_j + \sum_s \rho_s d_{sj} h_s - u_i \tau_{ij}) = 0, \qquad (2.3)$$

where $i = 1, 2, 3$, $(\rho_s, \rho u_i, \rho E)$ are the conserved variables, ρ_s are the partial densities with $k = 1, \ldots, N_s$ for a mixture of N_s species. The mixture total density, the pressure, and the total energy per unit volume are

$$\rho = \sum_s \rho_s, \quad p = RT\sum_{s=1}^{N_s}\frac{\rho_s}{M_s}, \quad \rho E = \sum_{s=1}^{N_s}\rho_s\left(e_s(T) + h_s^0\right) + \frac{1}{2}\rho v^2, \qquad (2.4)$$

where R is the universal gas constant, h_s^0 are the species formation enthalpies, and M_s

are the species molar masses. The viscous stress tensor is

$$\tau_{ij} = \mu \left(\frac{\partial u_i}{\partial x_j} + \frac{\partial u_j}{\partial x_i} \right) - \mu \frac{2}{3} \frac{\partial u_k}{\partial x_k} \delta_{ij}. \tag{2.5}$$

The diffusion flux is

$$d_{sj} = -D_s \frac{\partial X_s}{\partial x_j}, \tag{2.6}$$

where D_s is the diffusion coefficient and X_s is the mole fraction of species s. The conductive heat flux is

$$q_j = -\lambda \frac{\partial T}{\partial x_j}, \tag{2.7}$$

where λ is the thermal conductivity of the mixture. The chemical source term is

$$\Omega_s = M_s \sum_{r=1}^{N_r} (b_{s,r} - a_{s,r}) \left[k_{f,r} \prod_{m=1}^{N_s} \left(\frac{\rho_m}{M_m} \right)^{a_{m,r}} - k_{b,r} \prod_{m=1}^{N_s} \left(\frac{\rho_m}{M_m} \right)^{b_{m,r}} \right], \tag{2.8}$$

where a and b are the stoichiometric coefficients, and the forward reaction rate coefficients k_{fr} are given by Arrhenius' law:

$$k_{fr} = A_{f,r} T^{n_{f,r}} \exp(-E_{f,r}/kT) \tag{2.9}$$

The backward reaction rate coefficients are computed as $k_{b,r} = k_{f,r}/K_{c,r}^{eq}$. where $K_{c,r}^{eq}$ is the equilibrium constant

3. Computation Results

All the computations employ the multi-dimensional high order single/overset grid nonequilibrium code ADPDIS3D (Lani *et al.* 2013; Sjögreen & Yee 2009). 1D and 2D simplifications of the 3D EAST problem are considered using a single block option in the code. In addition, a one-temperature model is used, though the two-temperature model is required in order to obtain better agreement with the experiments. For the 2D case, axisymmetric geometry is not used as this option has not been implemented into AD-PDIS3D; planar geometry is used instead. The MUTATION library (Panesi *et al.* 2011), developed by Thierry Magin and Marco Panesi, is used to provide reaction rates and transport properties. We shall compare the results obtained by several standard shock-capturing methods and their filter counterpart schemes (Yee & Sjögreen 2007, 2010) for the early time evolution of the flow. Note that, for this viscous simulation, all the CFL values are based on the convection and viscous parts of the PDEs. Unless indicated, all shock-capturing schemes use the Roe average states.

3.1. *1D EAST simulation results*

The computational domain has a total length of $8.5 \, m$. The left side of the domain, with length $0.1 \, m$, is a high pressure region. The right side of the domain, with length $8.4 \, m$, is a low pressure region. The temperature in the vicinity of the shock can reach more than $20,000 \, K$, therefore ionized species must be taken into account. Here we consider the gas mixture as consisting of 13 species: e^-, He, N, O, N_2, NO, O_2, N_2^+, NO^+, N^+, O_2^+, O^+, He^+.

The initial conditions of the high and low pressure regions are listed in the table 1. The initial driver gas temperature is taken to be $6000 \, K$, as in McCorkle & Hassan (2010), and the pressure $p = 12.7116 \, MPa$ is chosen to obtain a shock velocity of approximately
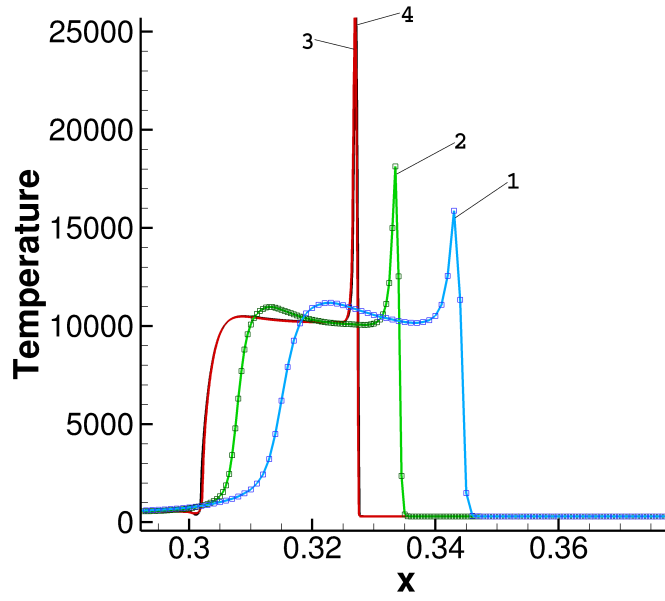
D.V. Kotov et al.

FIGURE 1. 1D, 13 species EAST problem: Second-order Harten-Yee TVD simulation for four levels of grid refinement with $CFL = 0.8$ and $t_{end} = 3.25 \times 10^{-5}$ *sec*. The Δx grid refinement study is: 10^{-3} *m* (line 1), 5×10^{-4} *m* (line 2), 5×10^{-5} *m* (line 3), 2.5×10^{-5} *m* (line 4).
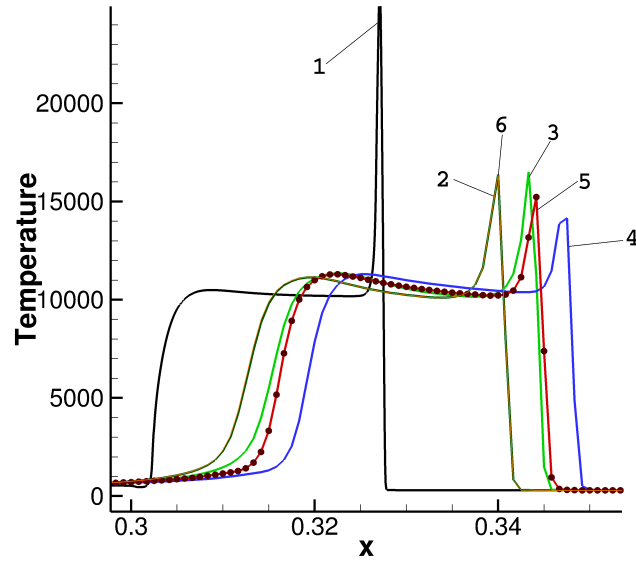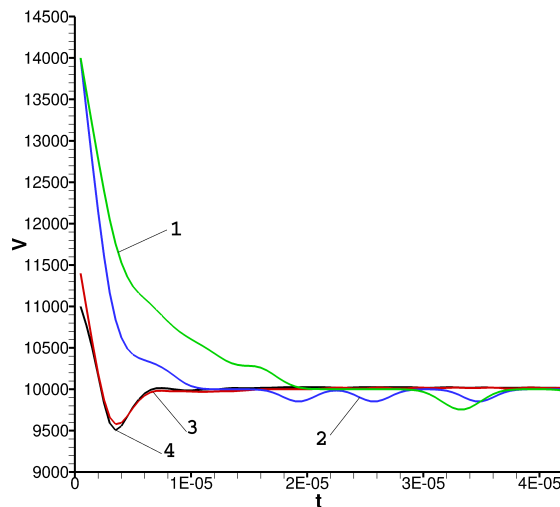

FIGURE 2. 1D, 13 species EAST problem: Comparison among 5 methods using 501 point grids with $CFL = 0.8$ and $t_{end} = 3.25 \times 10^{-5}$ *sec*. Reference solution (TVD on a $10,001$ point grid) (line 1), TVD (line 2), TVDafi+split (line 3), WENO5-llf (line 4), WENO5Pafi+split (line 5), TVD/SR (line 6). See text for method notation.

ρ	1.10546 kg/m^3		ρ	$3.0964 \times 10^{-4} kg/m^3$
T	6000 K		T	300 K
p	12.7116 MPa		p	26.771 Pa
Y_{He}	0.9856		Y_{O_2}	0.21
Y_{N_2}	0.0144		Y_{N_2}	0.79

TABLE 1. High (left) and low (right) pressure region initial data

FIGURE 3. 1D, 13 species EAST problem: shock velocity time dependance solution using $\Delta t = 5 \times 10^{-7} sec$ on four Δx: 10^{-3} m (line 1), 5×10^{-4} m (line 2), 5×10^{-5} m (line 3), 2.5×10^{-5} m (line 4).

10 km/sec in our computation, which is a typical velocity observed in the experiment. For the left-side boundary an Euler (slip) wall condition is applied, and for the right-side a zero gradient condition is applied for all variables.

Uniform 1-D grids are used for these simulations. To save computational cost, an initial computational domain of $(-0.1, 0.4)$ m is generated. During the computation the shock location is calculated at each time step. When the shock is close enough to the the right boundary, the computational domain is increased on the downstream side by 0.5 m.

Figure 1 shows the results from the computation using the Harten-Yee second-order TVD scheme (Yee 1989; Yee *et al.* 1990) for four grids with $\Delta x = 10^{-3}$ m, 5×10^{-4} m, 5×10^{-5} m and 2.5×10^{-5} m at time $t_{end} = 0.325 \times 10^{-4}$ sec. One can observe a significant shift in the shear (left discontinuity) and the shock (right discontinuity) locations as the grid is refined. The distance between the shear and the shock shrinks as the grid is refined. The difference between shock locations obtained on the grids with $\Delta x = 5 \times 10^{-5}$ m and 2.5×10^{-5} m is less than 0.3%. Thus the solution using $\Delta x = 5 \times 10^{-5}$ m can be considered as the reference solution.

Figure 2 shows a comparison between each of the five methods obtained on a coarse grid $(\Delta x = 10^{-3})$ m, along with the reference solution. The scheme labels are defined as follows:
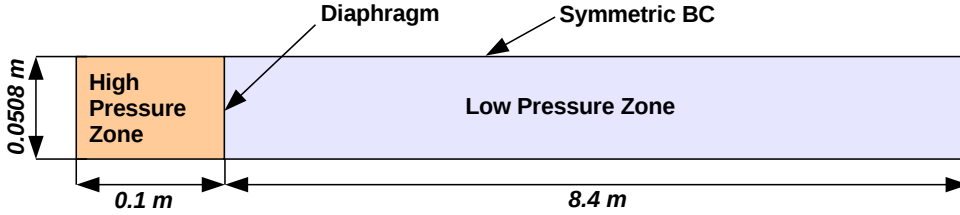
FIGURE 4. Computational domain for the 2D EAST problem.

• TVDafi+split: Sixth-order central base scheme with the Ducros *et al.* (2000) splitting of the governing equations. The flow sensor for the filter step is based on the shock and shear locations instead of using wavelets. See Yee & Sjögreen (2007, 2010) for further information on filter schemes.

• WENO5-llf: Fifth-order WENO (WENO5) using the local Lax-Friedrichs flux.

• WENO5Pafi+split: Nonlinear filter counterpart of the positive WENO5 using the local Lax-Friedrichs flux. The flow sensor for the filter step is based on the shock and shear locations instead of using wavelets. For the finite difference form of the positive WENO5-llf, see Zhang & Shu (2012).

• TVD/SR: Finite difference scheme with subcell resolution (Wang *et al.* 2012) using the Harten & Yee TVD scheme as the convection difference operator in the fractional step method. The Wang et al. new high order finite difference method with subcell resolution procedure was developed for a single reaction to overcome the wrong propagation speed of discontinuities for stiff source terms. Here we apply the subcell resolution method on one of the reaction coefficients to observe its performance.

Among the considered schemes, Fig. 2 indicates that the least dissipative scheme predicts the shear and shock locations best when compared with the reference solution. The results indicate that TVDafi+split is slightly more accurate than WENO5-llf. This is due to the fact that TVDafi+split reduces the amount of numerical dissipation away from high gradient regions. The test of using the subcell resolution method by applying it to only one of the reactions in this multireaction flow, does not improve the performance over standard schemes.

Figure 3 shows the shock velocity time dependence obtained on the four levels of grid refinement with $\Delta x = 10^{-3}$ m, 5×10^{-4} m, 5×10^{-5} m, and 2.5×10^{-5} m. The shock velocity is computed by taking a numerical derivative of the shock location as a function of time with some smoothing. During the first 5×10^{-6} sec the computed velocity has a strong dependence on the grid. After this initial duration, the computed velocities on the four grids asymptotically approach the same level. The result suggests that the major contribution to the error in shock location obtained on the coarse grid is due to the first 5×10^{-6} sec. A similar behavior has been observed by other authors; see e.g., Jacobs (1994); Petrie-Repar (1997) for the perfect gas case.

3.2. *2D EAST simulation results*

For the 2D case the computational domain in y is half of the 2D shock tube height. It has total length 8.5 m and height 0.0508 m (see Fig. 4). Other parameters and initial conditions of the high and low pressure regions are the same as for 1D case. The bottom boundary is treated as an isothermal wall with the constant temperature $T_{wall} = 300$ K. The top boundary is treated as a symmetrical boundary condition.
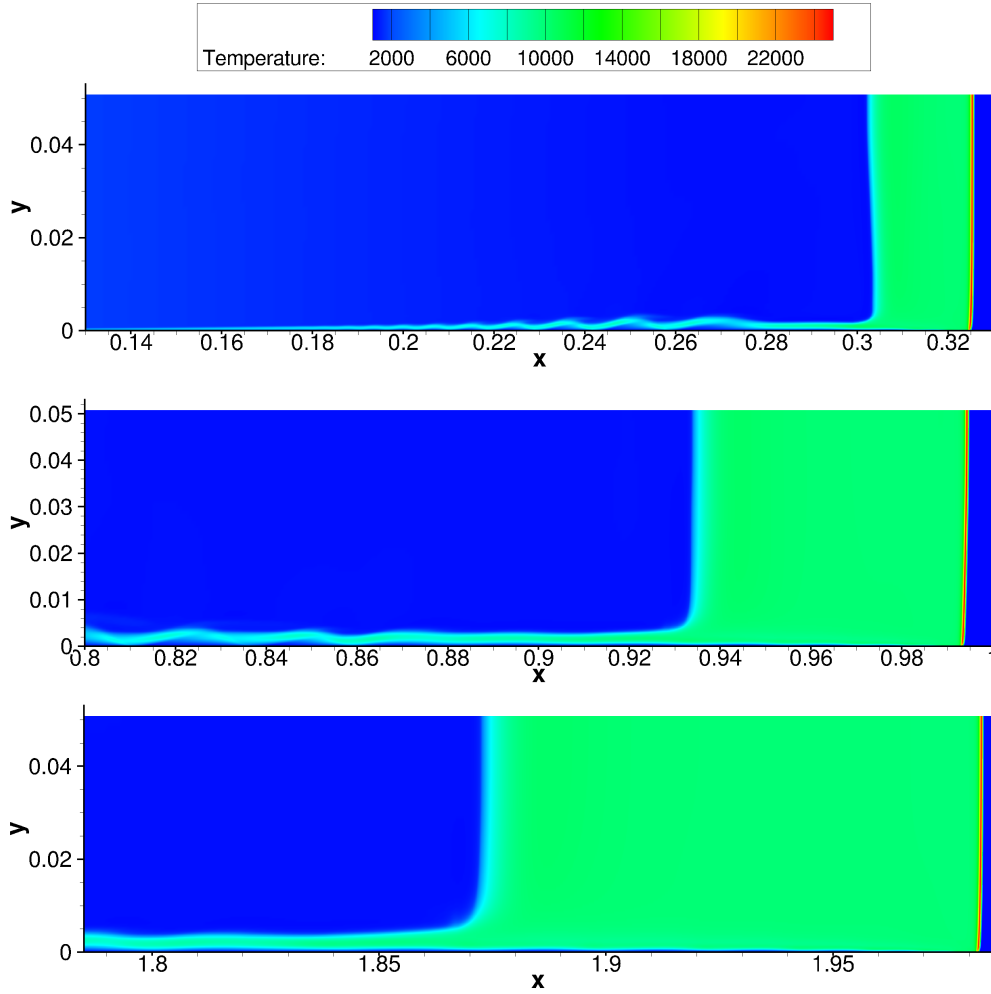
FIGURE 5. 2D, 13 species EAST simulation using TVD for $CFL = 0.7$ on a grid with clustering between shear and shock. Temperature contours for t_{end} from top to bottom: $3.25 \times 10^{-5} sec$, $10^{-4} sec$, $2 \times 10^{-4} sec$.

In the x-direction both uniform and non-uniform grids are used for these simulations. For uniform grids the same strategy is applied in the x-direction as for the 1D case. For non-uniform grids the shock and shear locations are computed for each timestep, and the grid points are clustered in the x-direction between the shear and shock locations with some tolerance to avoid interpolation errors during the re-grid process. This clustered portion of the grid moves as time advances. A grid stretching is also applied to smooth the transition from coarse to fine grid zone. At each time step the shock and shear locations are analyzed. If the shock/shear positions change by a prescribed distance, a re-grid is invoked and the data is interpolated onto the new grid. Note that in our case the interpolation is needed only in the vicinity of the transition between coarse and fine grid zones. The shock and shear locations are computed far away from the boundary layer. However, as the boundary layer develops, the shear layer becomes more curved so that
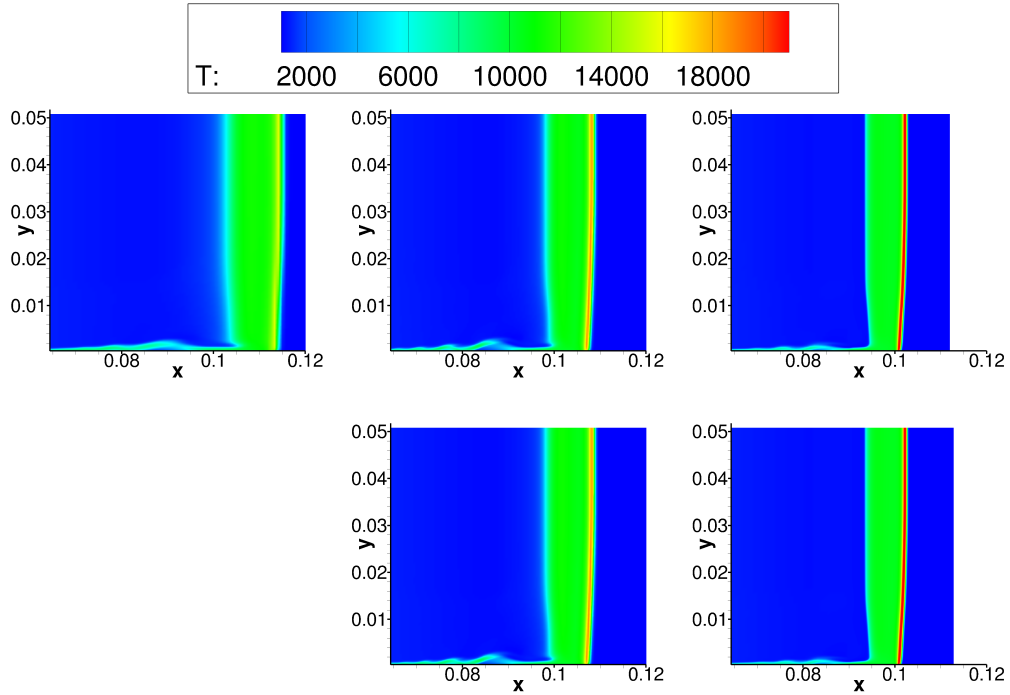
FIGURE 6. 2D, 13 species EAST simulation using TVD for $CFL = 0.7$ and $t_{end} = 10^{-5} sec$: Top Row: Three x-direction grid refinements: 601×121, 1201×121 and grid clustering between shear and shock in the x-direction (691×121 total). All y-grids use boundary grid stretching with a minimum of $\Delta y = 10^{-5}$ m. Bottom Row: Two x-direction grid refinements: 1201×121 and grid clustering between shear and shock in the x-direction (691×121 total). All y-grids use boundary grid stretching with a minimum of $\Delta y = 5 \times 10^{-6}$ m.

the tolerance for the shear side of the grid-clustering zone is increased. In the y-direction all grids use the same stretching algorithm, so that the grid points are clustered in the vicinity of the boundary layer.

The temperature contours computed for the times $t_{end} = 3.25 \times 10^{-5}$ sec, $t_{end} = 10^{-4}$ sec and $t_{end} = 2 \times 10^{-4}$ sec are shown in Fig. 5. The solution is obtained on the grid with clustering between the shear and the shock. The grid spacing parameters are $\Delta x_{min} = 5 \times 10^{-5}$ m, $\Delta x_{max} = 8 \times 10^{-4}$ m, $\Delta y_{min} = 10^{-5}$ m.

For this 2D test case it is not practical to obtain a very accurate reference solution due to the CPU-intensive nature of the problem. Here, three levels of refinement are conducted. Figure 6 shows the computed temperature contour results at time $t_{end} = 10^{-5}$ sec using $CFL = 0.7$ with TVD for three levels of x- and y-direction grid refinement. The top row shows three x-direction grid refinements of 601×121, 1201×121, and grid clustering between shear and shock in the x-direction of 691×121. The minimum grid step in the x-direction for the grid clustering is $\Delta x_{min} = 5 \times 10^{-5}$ m. All y grids use boundary grid stretching with a minimum of $\Delta y = 10^{-5}$ m. The bottom row shows the same two x-direction grid refinements 1201×121 and grid clustering between shear and shock in the x-direction of 691×121 (fine block). All y grids use boundary grid stretching with a minimum of $\Delta y = 5 \times 10^{-6}$ m. Comparing the two rows of the grid refinement study indicates that refining the x-direction grid, keeping the y-direction the same, has a
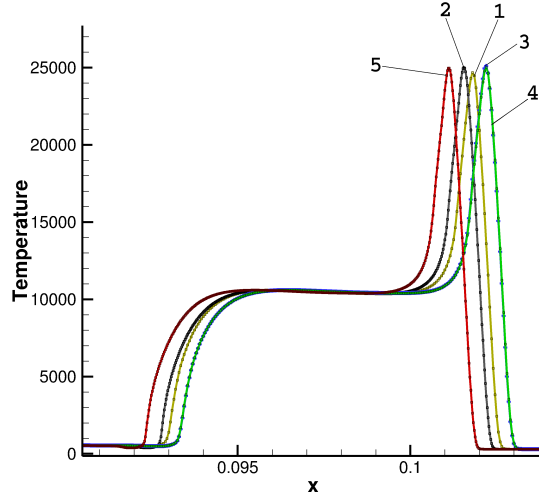
FIGURE 7. 1D and 2D, 13 species EAST simulations using TVD for $t_{end} = 3.25 \times 10^{-5} sec$:
1D, $\Delta x = 5 \times 10^{-5}$ m (line 1), 1D, $\Delta x = 2.5 \times 10^{-5}$ m, (line 2), 2D,
$\Delta x_{min} = 5 \times 10^{-5}$ $m, \Delta y_{min} = 10^{-5}$ m (line 3), 2D, $\Delta x_{min} = 5 \times 10^{-5}$ $m, \Delta y_{min} = 5 \times 10^{-6}$ m
(line 4), 2D, $\Delta x_{min} = 2.5 \times 10^{-5}$ $m, \Delta y_{min} = 10^{-5}$ m (line 5). All 1D simulations are on a
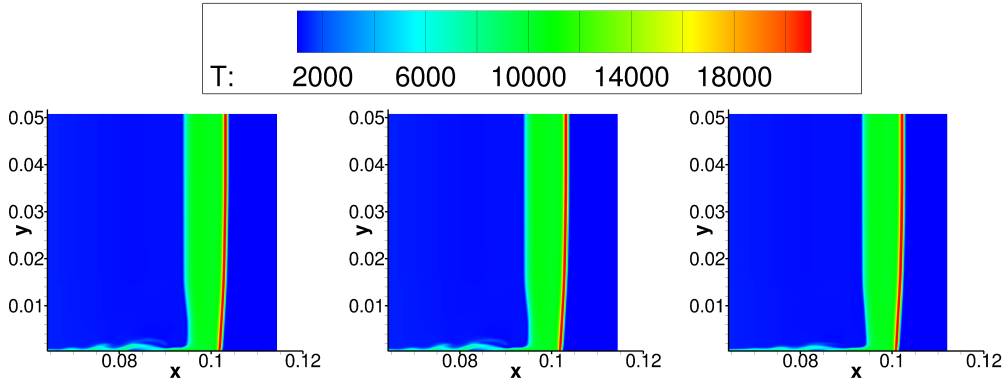uniform grid and all 2D simulations are on grids with clustering between shear and shock.

FIGURE 8. 2D, 13 species EAST simulation for $t_{end} = 10^{-5} sec$ on the same grid with refinement
between the shear and the shock: WENO5-llf for $CFL = 0.2$ (left), WENO5P-llf for $CFL = 0.4$
(center) and TVD $CFL = 0.7$ (right).

big effect on the locations of the shear and shock. This is due to the fact that aside from
inside the boundary layer, the shear and shock are nearly one dimensional. However,
comparing the last two columns of the grid refinement study indicates that refining
the y-direction grid, keeping the x-direction the same, has no effect on the locations
of the shear/shock, but improves the boundary layer prediction. As in the 1D EAST
simulation, the discontinuity locations shift as the x-direction grid is refined, and the
distance between the shear and the shock shrinks as the grid is refined. The shear and
shock strengths are also different. Table 2 indicates the maximum shear and contact
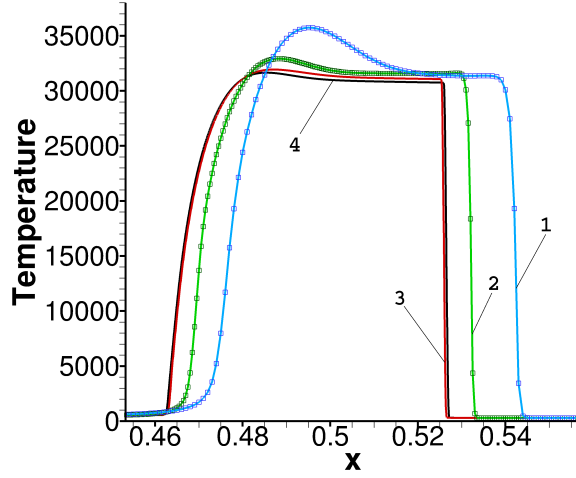temperature for each set of grids. For the minimum grid stretching of $\Delta y = 10^{-5}$ m,

FIGURE 9. 13 species 1D EAST problem with zero source term. For notation see Figure 1.

Grid N_x	601	1201	1201	691	691
Cluster in x	no	no	no	yes	yes
Min $\Delta y, m$	10^{-5}	10^{-5}	5×10^{-6}	10^{-5}	5×10^{-6}
Shock T_{max}, K	15,846	18,851	18,848	25,098	25,015
Shear T_{max}, K	11,301	11,203	11,203	10,598	10,598

TABLE 2. Shock and Shear maximum temperature grid dependence at time $t_{end} = 10^{-5} sec$. N_x indicates the grid spacing in the x-direction. The last two columns are grid clustering results for two different minimum y-grid stretching.

the maximum shear temperature is $11,300K$, and the maximum shock temperature is $15,846K$ for the 601×121 grid. However, the shear and shock strengths have a maximum shear temperature of $11,200K$ and a maximum shock temperature of $18,851K$ for the 1201×121 grid. For the stretched grid the shear and shock strengths have a maximum shear temperature of $10,600K$ and maximum shock temperature of $25,098K$. As we decrease the minimum grid stretching to $\Delta y = 5 \times 10^{-6} \ m$, the shear and shock strengths have a maximum shear temperature of $11,200K$ and a maximum shock temperature of $18,848K$ for the 1201×121 grid. For the stretched grid the shear and shock strengths have a maximum shear temperature of $10,600K$ and a maximum shock temperature of $25,015K$. Aside from the different shock/shear locations, the results in the last column show that the maximum temperature at the shock location is higher than the result indicated in the the middle and the first columns.

To ensure that grid clustering with $\Delta x_{min} = 5 \times 10^{-5} \ m$ is enough in terms of shock location error, we performed a computation on a grid twice-refined in the x-direction. The comparison of these results and a similar computation for the 1D problem are shown in Fig. 7. The 2D result profiles are taken on the upper boundary of the computational domain, where they have the best correspondence with the 1D case. The 2D results with the same Δx but different values of Δy almost coincide. The difference in the shock location for all five profiles does not exceed 1%.

The comparison among three numerical schemes is shown in the Fig. 8. The three

methods are regular TVD for $CFL = 0.7$, regular WENO5 with Lax-Friedrichs flux (WENO5-llf) for $CFL = 0.2$ and a positivity preserving version of WENO5-llf (Zhang & Shu 2012), designated as WENO5P-llf, for $CFL = 0.4$. It is well known that WENO-llf is very diffusive. That results in larger errors in the shock location, as can be observed in Fig. 8. WENO5P-llf obtains results similar to regular WENO5-llf, but it appears to be stable even for higher CFL numbers, for which regular WENO5-llf obtains an oscillatory solution.

4. Conclusions

The present study demonstrates some important numerical challenges affecting the accuracy of 1D and 2D numerical solutions in simulations of NASA EAST experiments. In the early stages of the time evolution, at around T= 10^{-5} sec, the importance of obtaining very high accuracy of the discontinuities, in order to avoid an overestimation of the shock velocity, has been shown. For the 2D case, to obtain high resolution results, a moving grid with grid clustering only in key regions of the computational domain is needed in order to avoid the use of the full computational domain and unnecessary grid clustering for the entire time evolution. The cause of the observed grid-dependence of the numerical solution is not fully understood and requires further investigation. One conjecture for the spurious behavior might be the stiff source terms, or, at least, the grid dependence may be amplified when the stiffness of the considered Ω_s is high enough. As discussed in (Wang *et al.* 2012; Yee *et al.* 2012) the level of grid- and scheme-dependence for obtaining the correct locations of discontinuities is normally dictated by the degree of stiffness of the source terms and the accuracy and amount of numerical dissipation contained in the scheme. Figure 9 shows the results of the same computation as in Fig. 1, but with zero source terms Ω_s. A similar behavior is observed. In this case it appears that the problem is not physically realistic, especially when both the shear and shock jumps are extremely high. The present study also indicates the danger in practical numerical simulations for problems containing stiff source terms where there is no reliable means of assessing the accuracy of the computed result other than by extreme grid refinement, which may be beyond the capability of current supercomputers. Another alternative would be to develop methods that obtain the correct speed of discontinuities on coarse grids, e.g. using ideas similar to (Wang *et al.* 2012). This approach might be very useful when there is a need to perform 3D computations for such experimental facilities as EAST. Future investigation is planned.

REFERENCES

DUCROS, F., LAPORTE, F., SOULÈRES, T., GUINOT, V., MOINAT, P. & CARUELLE, B. 2000 High-order fluxes for conservative skew-symmetric-like schemes in structured meshes: Application to compressible flows. *J. Comput. Phys.* **161**, 114–139.

GRIFFITHS, D., STUART, A. & YEE, H. 1992 Numerical wave propagation in hyperbolic problems with nonlinear source terms. *SIAM J. Numer. Anal.* **29**, 1244–1260.

JACOBS, P. A. 1994 Numerical simulation of transient hypervelocity flow in an expansion tube. *Computer & Fluids* **23**, 77–101.

LAFON, A. & YEE, H. 1996 Dynamical approach study of spurious steady-state numerical solutions for nonlinear differential equations, part III: The effects of nonlinear source terms in reaction-convection equations. *Comput. Fluid Dyn.* **6**, 1–36.

LANI, A., SJÖGREEN, B., YEE, H. C. & HENSHAW, W. D. 2013 Variable high-ordermultiblock overlapping grid methods for mixed steady and unsteady multiscale viscous flows, part II: Hypersonic nonequilibrium flows. *Commun. Comput. Phys.* **13**, 583–602.

LEVEQUE, R. & YEE, H. C. 1990 A study of numerical methods for hyperbolic conservation laws with stiff source terms. *J. Comp. Phys.* **86**, 187–210.

MCCORKLE, E. & HASSAN, H. 2010 Study of radiation in electric arc shock tubes. In *10th AIAA/ASME Joint Thermophysics and Heat Transfer Conferencee*. Chicago, Illinois.

PANESI, M., MAGIN, T., BOURDON, A., BULTEL, A. & CHAZOT, O. 2011 Study of electronically excited state populations of atoms and molecules predicted by means of a collisional-radiative model for the fire II flight experiment. *Journal of Thermophysics and Heat Transfer* **25** (25), 361–374.

PETRIE-REPAR, P. 1997 Numerical simulation of diaphragm rupture. PhD thesis, University of Queensland.

SJÖGREEN, B. & YEE, H. C. 2009 Variable high order multiblock overlapping grid methods for mixed steady and unsteady multiscale viscous flows. *Commun. Comput. Phys.* **5**, 730–744.

WANG, W., SHU, C., YEE, H. C. & SJÖGREEN, B. 2012 High order finite difference methods with subcell resolution for advection equations with stiff source terms. *J. Comput. Phys.* **231**, 190–214.

YEE, H., KOTOV, D., WANG, W. & SHU, C.-W. 2012 Spurious behavior of shock-capturing methods: Problems containing stiff source terms and discontinuities. In *Proceedings of the ICCFD7*. The Big Island, Hawaii.

YEE, H. & SJÖGREEN, B. 2007 Development of low dissipative high order filter schemes for multiscale navier-stokes/mhd systems. *J. Comput. Phys.* **225**, 910–934.

YEE, H. C. 1989 *A class of high-resolution explicit and implicit shock-capturing methods*. VKI lecture series 1989-04.

YEE, H. C., KLOPFER, G. H. & MONTAGNE, J.-L. 1990 High-resolution shock-capturing schemes for inviscid and viscous hypersonic flows. *J. Comput. Phys.* **88**, 31–61.

YEE, H. C. & SJÖGREEN, B. 2010 High order filter methods for wide range of compressible flow speeds. In *Proc. of ASTRONUM-2010*. San Diego, Calif, expanded version submitted to Computers & Fluids.

YEE, H. C., SJÖGREEN, B., SHU, C., WANG, W., MAGIN, T. & HADJADJ, A. 2011 On numerical methods for hypersonic turbulent flows. In *Proc. of ESA 7th Aerothermodynamics Symposium*. Site Oud Sint-Jan, Brugge, Belgium.

ZHANG, X. & SHU, C.-W. 2012 Positivity-preserving high order finite difference weno schemes for compressible euler equations. *J. Comput. Phys.* **231**, 2245–2258.